Journal of Power Sources 214 (2012) 258–265

Contents lists available at SciVerse ScienceDirect

Journal of Power Sources

journal homepage: www.elsevier.com/locate/jpowsour

Phase-separated silicon–tin nanocomposites for high capacity negative electrodes in lithium ion batteries

Xingcheng Xiao [a,*], John S. Wang [b], Ping Liu [b], Anil K. Sachdev [a], Mark W. Verbrugge [a], Daad Haddad [c], Michael P. Balogh [a]

[a] General Motors Global R&D Center, 30500 Mound Road, Warren, MI 48090, USA
[b] HRL Labs, Malibu, CA 90265-4797, USA
[c] MEDA Engineering and Technical Services, LLC, Southfield, MI, USA

HIGHLIGHTS

- A phase separation-induced nanostructure (amorphous Si nanoparticles uniformly embedded in Sn matrix) was reported.
- The unique nanostructure improved fracture toughness and prevented the microcrack propagation during the cycling.
- The composite electrode showed excellent cycling stability and high capacity.
- The proposed concept can be generalized for material design to improve mechanical properties.

ARTICLE INFO

Article history:
Received 2 February 2012
Received in revised form
13 April 2012
Accepted 16 April 2012
Available online 27 April 2012

Keywords:
Ion battery
Nanocomposite
Si–Sn alloy
Phase separation

ABSTRACT

Both silicon and tin have a high specific capacity (3600 mAh g^{-1} for $Li_{15}Si_4$ and 992 mAh g^{-1} for $Li_{22}Sn_5$ respectively) and are among the most attractive materials for potential negative electrodes in lithium ion batteries. However, mechanical degradation induced by the large volume expansion during the cycling has limited their practical application. In this work, we developed a new class of Si–Sn nanocomposites with unique phase-separated nanostructure, where the amorphous Si nanoparticles are thermodynamically precipitated out from Si–Sn alloy and embedded within the Sn matrix. The phase separation-induced nanostructure provides the capability to mitigate the mechanical degradation, by preventing the nucleation and propagation of microcracks during lithiation. The nanocomposite electrode exhibits relative high capacity (1400 mAh g^{-1}) and excellent cycling stability with the optimum composition and nanostructure.

1. Introduction

The lithium ion battery is the most promising energy storage system for meeting the demands of electric and hybrid electric vehicles. Significant efforts have been made to improve the energy and power density, as well as to extend lifetime. Much work is continuing to develop new materials to improve the specific capacity of both the negative electrode and the positive electrode. Although the positive electrode often has lower specific capacity, it is unlikely that significant progress can be made to improve positive electrode capacities by, for example, an order of magnitude, in the near future due to the limited amount of lithium that can be extracted in the unit crystal structure of known positive electrode materials. The negative electrode, on the other hand, is generally based on graphite, which has a specific capacity about 372 mAh g^{-1}. To obtain a noticeable improvement in the specific capacity of the Li-ion cells, it is important to replace the carbonaceous negative electrodes with materials having a specific capacity on the order of 1000–1200 mAh g^{-1} [1]. Indeed, a number of metals and semiconductors, including aluminum, tin and silicon, react with lithium and form alloys and can provide a specific capacity much larger than that obtained by conventional graphite [2]. However, the further capacity increases for negative electrodes will not significantly increase cell capacity unless accompanied by significant increases in positive electrode capacities [1,3].

Silicon (Si) has been considered as an alternative to commercial graphite as the negative electrode for lithium ion batteries. Silicon provides much higher specific capacity (3600 mAh g^{-1} $Li_{15}Si_4$) compared with graphite (372 mAh g^{-1} LiC_6). However, the volume change of up to 300 vol.% for Si during the lithiation (insertion) and

* Corresponding author. Tel.: +1 248 912 8132; fax: +1 586 986 9260.
E-mail addresses: xingcheng.xiao@gm.com, xcxiao@gmail.com (X. Xiao).

0378-7753/$ – see front matter © 2012 Elsevier B.V. All rights reserved.
doi:10.1016/j.jpowsour.2012.04.028

delithiation (extraction) processes leads to fracture of the active Si materials and/or loss of electrical contact with the conductive additives or the current collectors [4,5]. Another attractive candidate, Sn (theoretical capacity up to 992 mAh g^{-1}), also has the same problem of a large volume expansion upon lithiation leading to rapid capacity degradation.

The basic mechanism responsible for the loss of capacity due to fracture of the electrode materials is the loss of electrical contact and the creation of new surfaces, which irreversibly consume the active lithium to form new solid electrolyte interfaces (SEI) [6,7]. Different approaches have been proposed to extend the cycle life of Si- and Sn-based electrodes, including pure micro- and nano-scaled powder dispersed in an inactive matrix, nanowires, or thin films, as summarized by Kasavajjula et al. [1]. All these approaches can be summarized as belonging to two categories: one to retain the amorphous state of the electrode materials during cycling, and the other to reduce the feature size down to the critical dimensions. Often, the amorphous phase can avoid a phase transformation, and, therefore, avoid the formation of phase boundaries where the cracks and fractures initiate. It has been demonstrated that an amorphous Si electrode has better performance than crystalline Si [1,5]. The other solution is to control the size of the particles or thin films to mitigate the stress within them. Based on fracture mechanics [8]:

$$a_c = \frac{2}{\pi}\frac{K_{1c}^2}{\sigma^2} \quad (1)$$

where the fracture toughness K_{1c} and yield strength σ in polycrystalline silicon are approximately 0.751 MPa $m^{-1/2}$ and 1.1 GPa, respectively, a critical flaw size a_c of around 300 nm is obtained, above which it is very likely that the Si particle will fracture during lithiation.

A problem associated with nanoscale materials is the large amount of SEI that will form on the high surface area, leading to a significant irreversible loss in capacity. This behavior essentially limits the practical application of nanoscale materials unless this SEI formation issue is resolved. Another research area is to develop Si- or Sn-based alloy electrodes that contain either an active or an inactive material that serves as a buffer layer and mitigates the fracture of Si or Sn. However, when inactive materials are used as the buffer phase, the specific capacity of the overall alloy could be significantly sacrificed because of the high mass of inert phase (for example, $CoSi_2$ 58 mAh g^{-1}, or $NiSi_2$ 198 mAh g^{-1} [3], are much lower than graphite itself). To develop high capacity electrodes, it would, therefore, be better to choose the lithium-active material as the secondary phase.

Dahn et al. [9,10] investigated the electrochemical performance of the $Si_{1-x}M_x$ binary system (where M = Sn, Ag, or Zn). One interesting result they showed was that the amorphous phase could be retained during cycling in the $Si_{1-x}Sn_x$ system (for $x < 0.5$), leading to the expectation that this could be used as the negative electrode. However, the cycling stability of these samples was not discussed.

In this paper, we demonstrate that Si and Sn are immiscible in each other, which agrees with the thermodynamic nature of Si and Sn and the Si–Sn binary phase diagram shown in Fig. 1. Our work suggests that the Si and Sn are phase separated and that a micro/nano-structure can be achieved by controlling the synthesis process to produce the phases to be below the critical size for the generation of microcracks. The ideal case would be to create nano-confined architectures, wherein the Si particles are separated by the Sn matrix. Such a microstructure could have several advantages: (1) the Sn is electrically conductive, which would help electrons reach the Si particles, (2) if a crack was generated in the

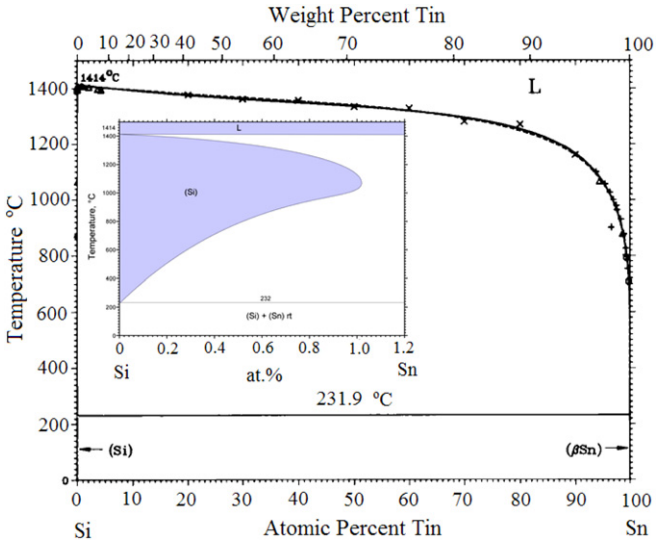

Fig. 1. The Si–Sn binary phase diagram.

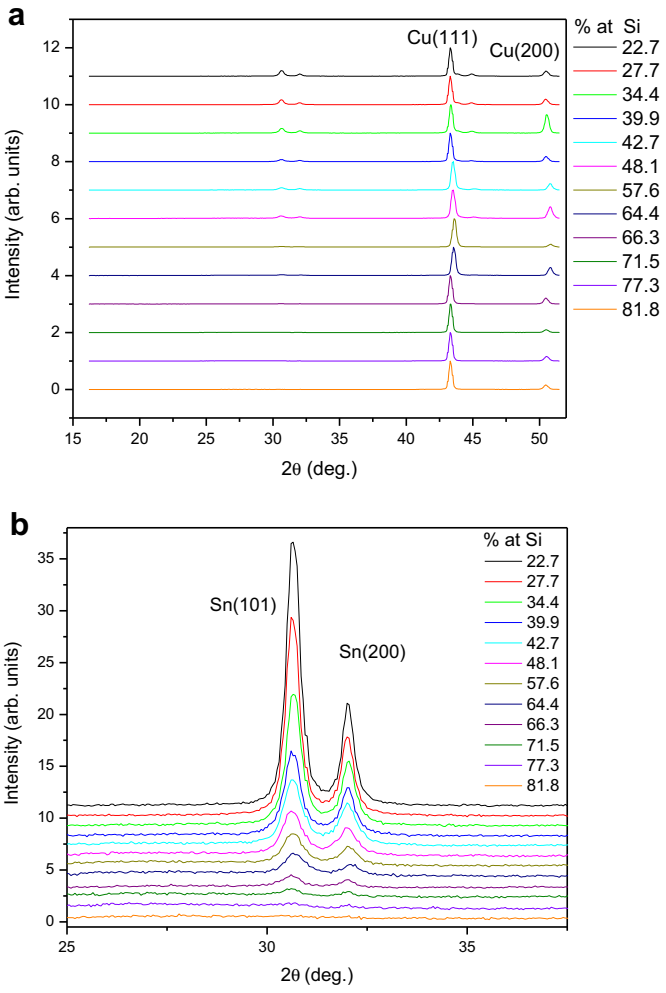

Fig. 2. XRD pattern of as-deposited Si–Sn thin films with different Si/Sn ratios deposited on a Cu substrate; (a) the wide range XRD diffraction shows no crystalline Si is present; (b) the relative intensity of diffraction from Sn with different Si/Sn ratios.

matrix, the soft Sn matrix could absorb the elastic strain energy and prevent the microcracks from propagating, and (3) the immiscible characteristics of Si and Sn and their phase separation could avoid electrochemical sintering and thus prevent coalescence of the particles that would otherwise lead to rapid mechanical degradation.

Based on these potential benefits, we used a sputtering system and a combinatorial approach to produce Si–Sn alloys with different ratios, from pure Si to pure Sn. We also investigated the electrochemical performance of these nanostructured samples along with their chemical and physical characteristics. This work has demonstrated that we can mitigate the mechanical degradation that occurs to the pure materials by tuning the Si/Sn ratio of the nanocomposite. We also demonstrate that at a specific Si/Sn ratio, phase separation occurs, and the electrode materials exhibit significant improvements in charge storage capability along with excellent cycling stability.

2. Experimental

Si and Sn were codeposited as a composite thin film in a Gamma 1000 sputtering system (Surrey NanoSystems, UK). A roughened copper foil was used to provide good adhesion between the Si–Sn thin films and the copper current collector. The deposition plasma for each constituent material (Si and Sn) was created with DC power applied to each of two magnetron guns under an argon flow of 14 sccm. The dynamic pressure during the growth of the films was 3 mTorr, and the substrate was kept at room temperature. The typical thickness of the thin film is around 1 μ.

Ex situ X-ray diffraction (XRD) was used to study the structure of the thin film deposited on the Cu current collector. All samples

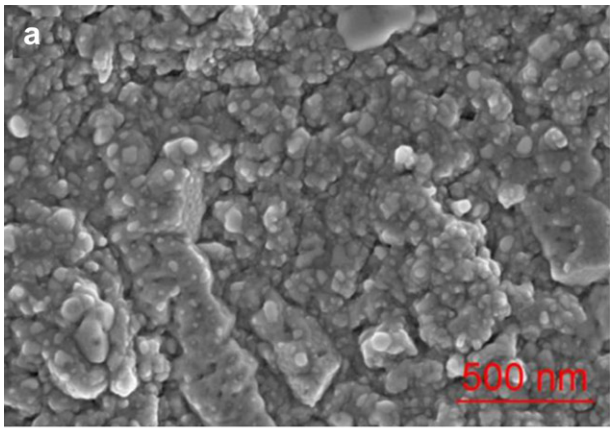

$Si_{40}Sn_{60}$

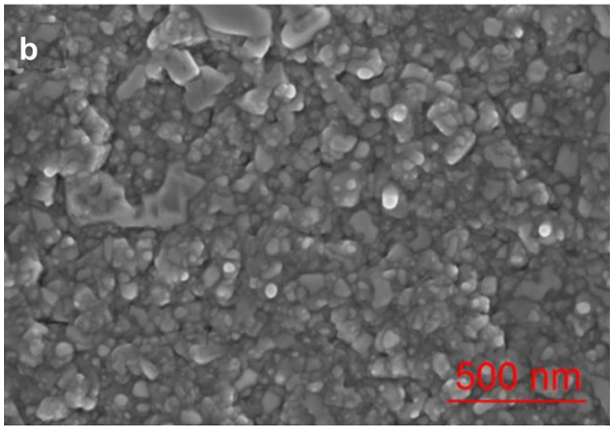

$Si_{48}Sn_{52}$

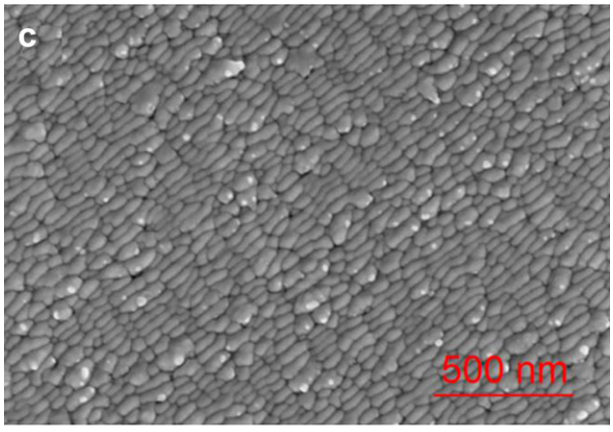

$Si_{68}Sn_{32}$

Fig. 3. Surface morphology of Si–Sn on Cu substrate.

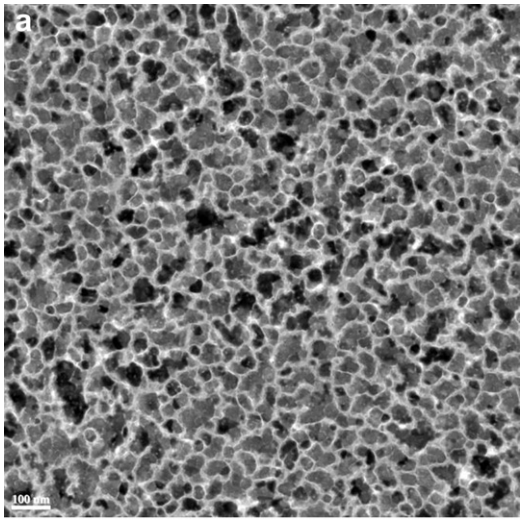

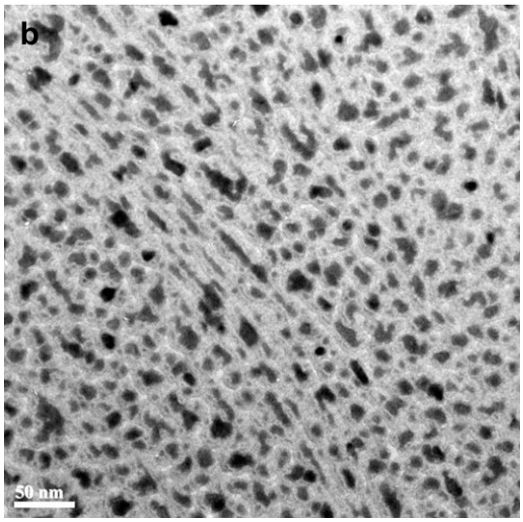

Fig. 4. HAADF-STEM images showing the phase separation between Si and Sn (Si is the darker phase and Sn is the brighter phase). (a) Higher Si content, (b) Lower Si content.

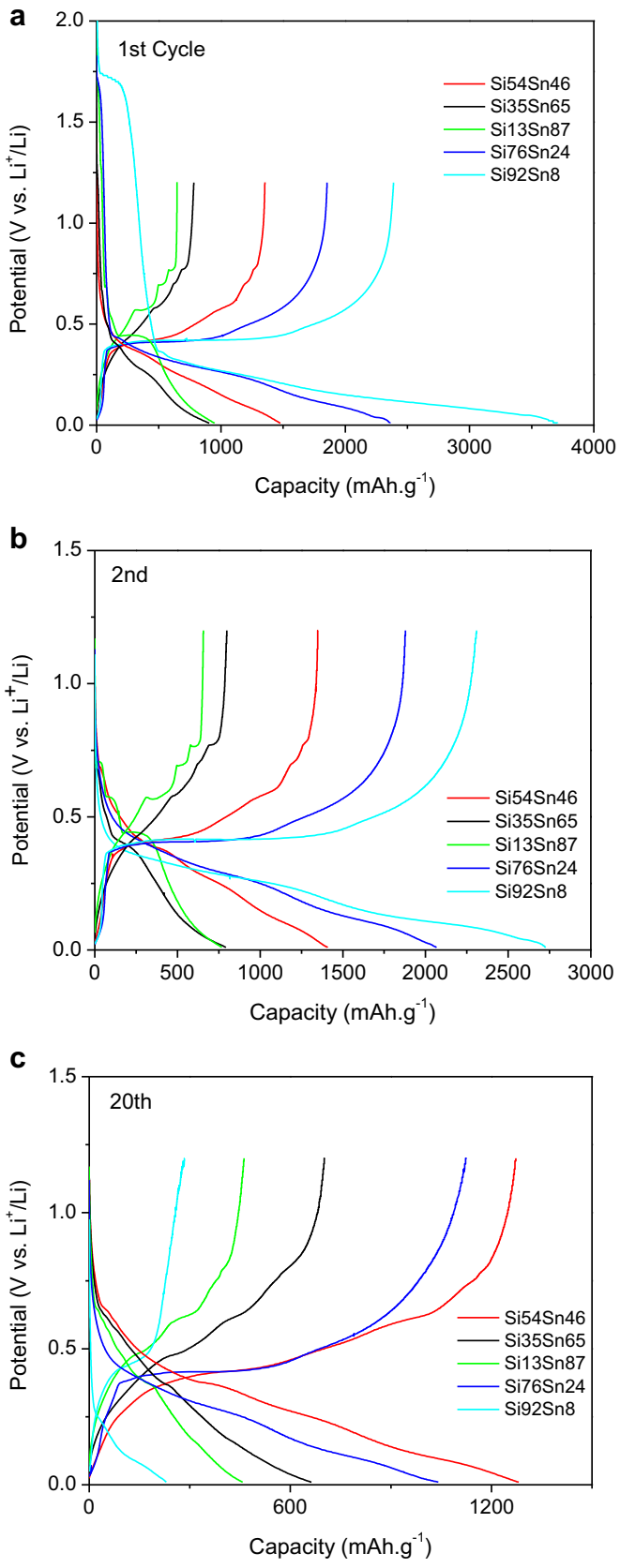

Fig. 5. Galvanostatic charge/discharge curves for Si–Sn thin films at different Sn/Si composition ratios at a rate of C/10; (a) 1st cycle; (b); 2nd cycle; (c) 20th cycle.

were examined using Cu-Kα radiation in a Bruker AXS general area detector diffractometer system (GADDS). The diffraction images were collected for a period of 5 min with a 0.5-mm collimator and a sample-to-detector distance of 150 mm. The composition of each sample pad was determined by electron probe microanalysis (EPMA), while selected samples were characterized with JEOL 2100F AC transmission electron microscope operating at 200 kV. Scanning transmission electron microscopy (STEM) images were collected using a high angle annular dark field (HAADF) detector.

All electrochemical experiments were carried out in Swagelok cells inside an Ar-filled glove box. Pure lithium metal was used for the counter electrode for the half-cell tests. The electrolyte solution was 1 M $LiPF_6$ in ethylene carbonate (EC) and dimethyl carbonate (DMC) (1:1 v/v). A Celgard 3501 (1 衿 micron thick microporous polypropylene film with 40% porosity) was used as the separator. Galvanostatic tests for all samples were performed with an Arbin BT-2000 battery testing station at a cycling voltage between 10 mV and 1.5 V (relative to a Li/Li^+ electrode).

3. Results and discussion

XRD results are summarized in Fig. 2. Other than the strong Cu diffraction peaks observed from the substrate, several Sn peaks were also detected, indicating that the Sn phase was crystalline, while no Si diffraction peaks were detected, indicating the amorphous nature of the Si. This is expected since the deposition temperature is too low for Si to develop a crystalline phase. No peaks representing any other Si–Sn phase were observed in any of the sputtered samples examined, which clearly demonstrated that the Si and Sn were phase separated, in agreement with the immiscibility of Si and Sn according to the phase diagram shown in Fig. 1. This nanostructure induced by phase separation is very critical to significantly improve its electrochemical performance. The overall mechanism for this will be explained in the following sections.

Based on the Scherrer equation [11], the average Sn crystallite size estimated from the various patterns in Fig. 2 was 20–50 nm; higher Si contents led to smaller Sn grains, as confirmed from the SEM images in Fig. 3, which show that the surface morphology associated with the Sn grain size becomes rougher with increasing Si content. With the high sensitivity to atomic number contrast, detailed insight was gained with HAADF-STEM imaging. As shown

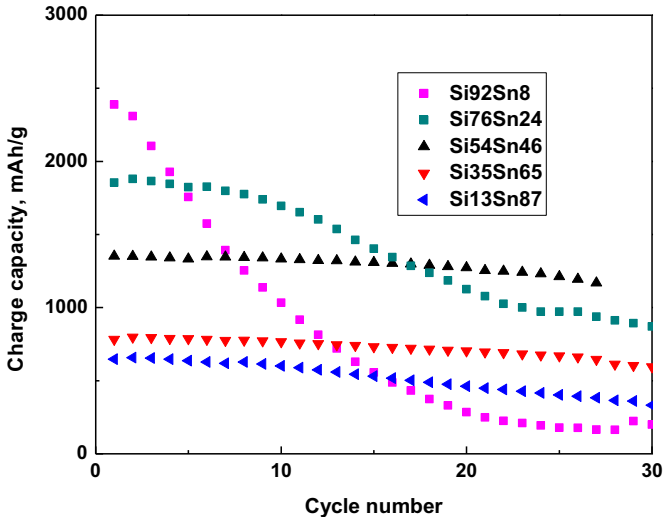

Fig. 6. The charge capacities of Si–Sn film electrodes at different Sn/Si composition ratios were plotted as a function of the cycle number.

Table 1
Summary of Coulombic efficiency.

	1st cycle irreversible loss, %	Average irreversible loss (10 cycles), %
Si_{92}/Sn_8	65	92
Si_{76}/Sn_{24}	79	96
Si_{54}/Sn_{46}	92	98
Si_{35}/Sn_{65}	86	99
Si_{13}/Sn_{87}	68	90

in Fig. 4, the phase separation between the Sn (bright features) and the Si (dark features) results in discrete amorphous Si nanoparticles dispersed in a continuous crystalline Sn matrix. The Si particle size ranged from 30 to 70 nm for high Si contents, with an average value of 50 nm, and decreased with decreasing amount of Si in the alloy. The Sn thickness between the Si particles was around 20 nm for the high Si content alloy, and increased with decreasing Si.

We first examined the effects of Si/Sn composition ratios on galvanostatic charge/discharge behaviors. A comparison of Si–Sn films with different Si/Sn composition ratios at a charge rate of C/10 is shown in Fig. 5a (1st cycle), b (2nd cycle), and c (20th cycle). During the initial cycle (Fig. 5a), the cell capacities are higher with increasing Si content, since the theoretical capacity of $Li_{15}Si_4$ (3580 mAh g^{-1}) is much larger than that of $Li_{4.4}Sn$ (992 mAh g^{-1}) [12]. However, at very high Si content (Sn_8Si_{92}), the capacity was lower (around 2400 mAh g^{-1}) suggesting that not all the Si is accessible to accommodate the Li-ions due to the dramatic volume change that occurs, and also the high intrinsic resistance of Si [5]. The voltage profiles of Si–Sn alloys also reflected the charge characteristics of each individual Si and Sn phase. For example, for a high Sn content, we can clearly observe multiple constant-voltage plateaus for crystalline Sn. These plateaus correspond to different solid-solution regions wherein each plateau represents regions of co-existence of two-phases: $Li_{22}Sn_5$–Li_7Sn_3, Li_7Sn_3–LiSn, LiSn–Li_2Sn_5, and Li_2Sn_5–Sn, during the Li^+ extraction process from 0 to 1 V [8]. As the Sn content decreases, the constant-voltage plateaus of Sn become less visible while a broad constant-voltage plateau becomes apparent near 0.4 V. This broad featureless voltage characteristic is a typical representation of amorphous Si during charge (Si alloy delithiation process) [9]. This distinguishing characteristic feature from both Si and Sn further demonstrates that the Si and Sn were phase separated from each other.

We also investigated the effects of Si/Sn composition ratios on cycling stability. Fig. 5c shows the charge characteristics of Si–Sn films after 20 cycles. The constant-voltage plateaus of crystalline Sn faded upon cycling indicating that the Sn is tending to became amorphous due to low atom mobility [13,14]. The cycling performance of all Si–Sn samples is also summarized in Fig. 6. While the capacity retention of 65:35 and 46:54 at.% (Sn:Si) ratios were better than those with high Si content, the 46:54 ratio was the most promising composition because of its high specific charge capacity. At 1400 mAh g^{-1}, the electrode reached 90% of its theoretical capacity (1550 mAh g^{-1}). This composition offers a good balance between electrical conductivity and the ability to accommodate the large volume expansion. Table 1 compares the Coulombic efficiency of the samples with different ratios. It shows that the cyclic efficiency of the sample with Si/Sn close to unity is better than other samples, which is consistent with the cycling stability.

Destructive physical analysis (DPA) was used to examine the electrodes after cycling. Fig. 7 presents optical images of the electrodes after cycling. These images show portions of the film on the samples with either high Sn or high Si to be delaminated; i.e., the shiny areas representing the exposed copper current collector, compared with the black area corresponding to the thin film electrode that still covers the current collector. On the other hand, the samples closer to the 50:50 Sn:Si distribution still had most of the film attached to the Cu current collector. A detailed examination of the remaining parts on the current collectors revealed different crack patterns, shown in the SEM images in Fig. 8. The sample with a high Si content showed most of the delaminated debris to be loosely bonded to the current collector, indicating poor

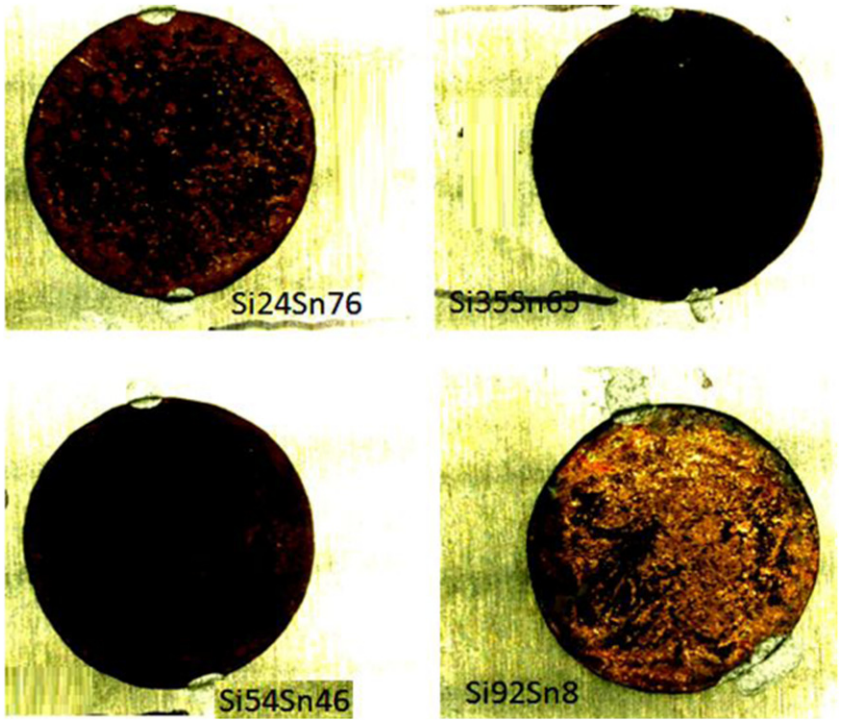

Fig. 7. The optical images of Si–Sn electrode after cycling.

electric contact and low capacity, compared with the apparent robust coating on the Si–Sn samples with low Si content.

A closer examination of the charge/discharge response upon cycling enables one to distinguish the capacity fading behavior of each individual material and provide important insight into the aging mechanisms. We used the differential capacity versus voltage correlation (dQ/dV vs. V) to amplify the effect of voltage profile on Si–Sn composition ratio during cycling. Fig. 9 shows this correlation for different composition Si–Sn films at the1st, 2nd, and 20th cycle. The peaks in these curves represent the potential dependent charge storage at constant-voltage (solid-solution co-phase) regions during delithiation. The area under the peaks reflects the total stored charge at those specific constant-voltage regions, with the taller peaks indicating a higher stored charge at those specific voltages. The Si peak is shown at 0.4 V while three Sn peaks are visible between 0.5 and 0.8 V. The Si peak is more evident when the Si content is greater than 50%, while the Sn peaks increase with increasing Sn content. Both the Si and Sn peaks were only observed together for the 46:54 Sn:Si sample.

All peaks became less visible after 20 cycles (Fig. 9 bottom). In particular, at 92% Si, the Si peak was no longer observed after 20 cycles, and the material lost 90% of its initial capacity. While the peaks became less visible for the 46:54 Sn:Si sample, the capacity retention was very good (Fig. 6). These results further suggest that Sn either becomes amorphous or the Sn particles become too small to form any long range crystal order.

4. Discussion

The Si–Sn system has been studied by Dahn et al. [9,15], who demonstrated that the amorphous Si–Sn alloy could have good performance. We did not, however, observe this amorphous feature, but, instead, obtained a phase-separated Si–Sn nanocomposite wherein the amorphous Si nanoparticles are embedded in the Sn matrix. Our results are consistent with the view that the synergetic effect of this nanostructure gives rise to the very good cycling performance that was observed. As demonstrated in our previous work [16], a negative electrode of pure Si normally degrades very quickly, due to the high volume expansion during lithiation. Sn particles, on the other hand, will form an interconnected network structure, as shown by in-situ X-ray transmission microscopy, and will not shrink back to the original shape [17]. This interlocking structure can behave like a sponge and accommodate the expansion of the Si nanoparticles at a lower

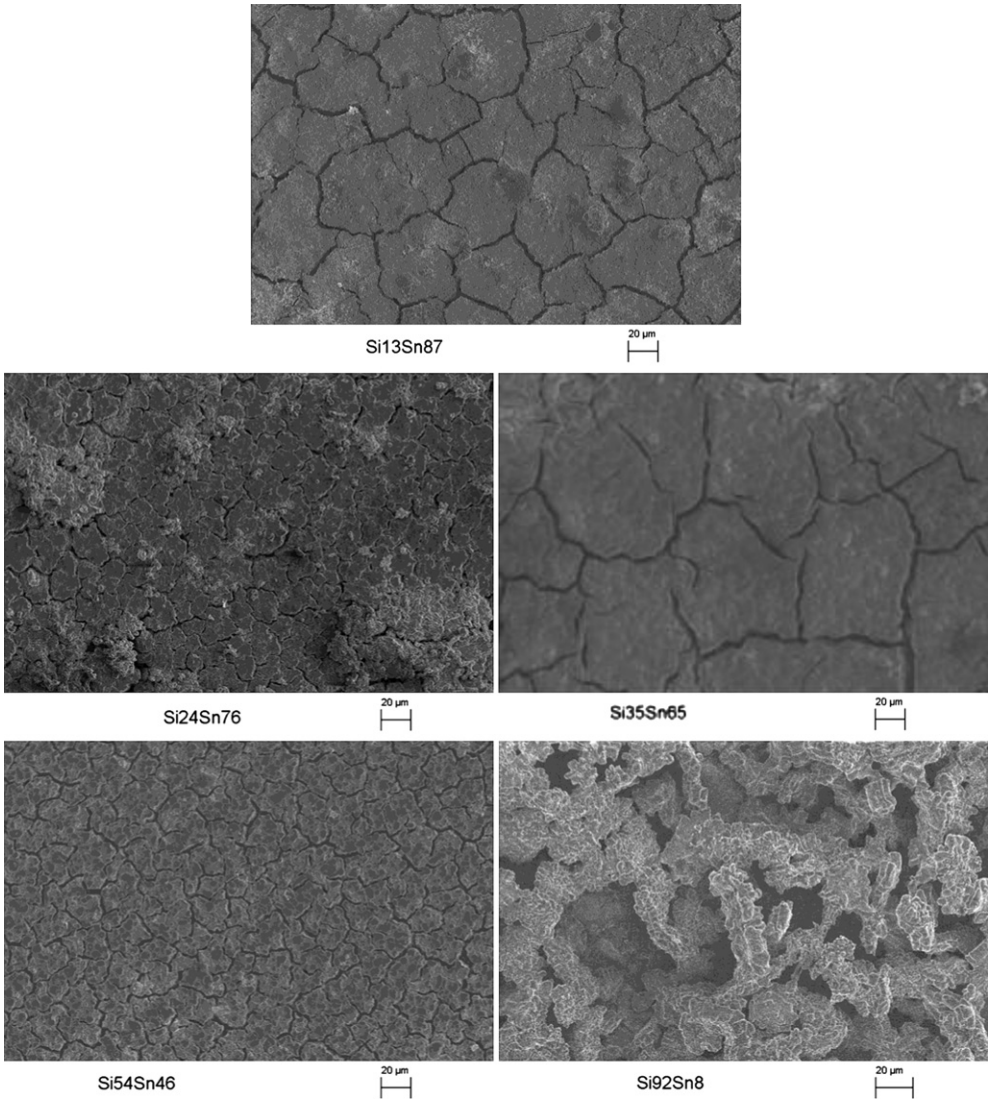

Fig. 8. SEM images of cycled samples.

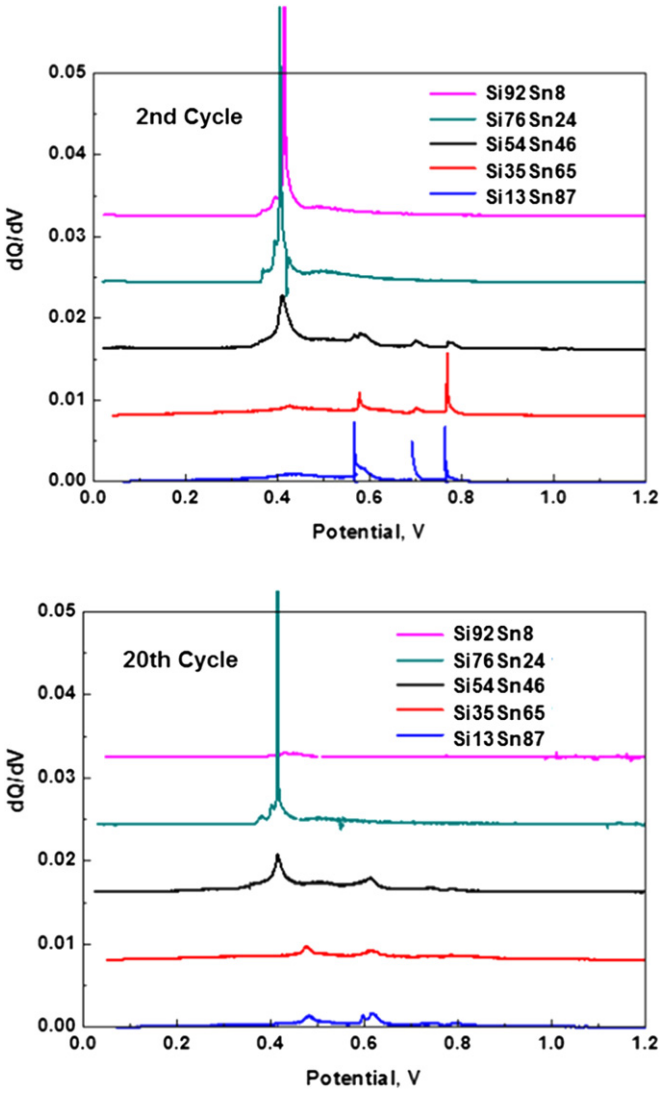

Fig. 9. Differential capacity versus voltage curves plotted for Si–Sn alloy samples with different Sn:Si composition ratios for 2nd cycle (top) and 20th cycle (bottom).

potential. Even though some microcracks may nucleate in the Sn matrix, the higher fracture toughness of Sn resists crack propagation. In addition, according to the d*Q*/d*V* data, the crystalline Sn becomes amorphous upon cycling, which, therefore, further hinders the non-isotropic volume expansions of the Si–Sn matrix. Last, we note that the Si phase has a particle size below 50 nm diameter, which may be below the critical size to cause particle cracking.

Prior research [18–20] on lithium ion diffusion-induced stress and its impact on nucleation and propagation of microcracks has shown that the large lithium concentration gradient through the radius of the particles, or along the thickness direction of the thin films, is most likely responsible for the stress to exceed the fracture strength of the material. In our case, once the Sn ratio in the film is beyond the percolation value, it will form an interconnected Sn phase, whose width is in the range of tens of nanometers. This nano-confinement effect can significantly improve the stability and toughness of Si within the Sn matrix, as schematically described in Fig. 10, which shows the torturous path for the microcrack to propagate in the phase-separated nanostructure.

Another attribute that benefits the cycling stability of the electrode is the fact that the insertion of Li into Si and Sn occurs

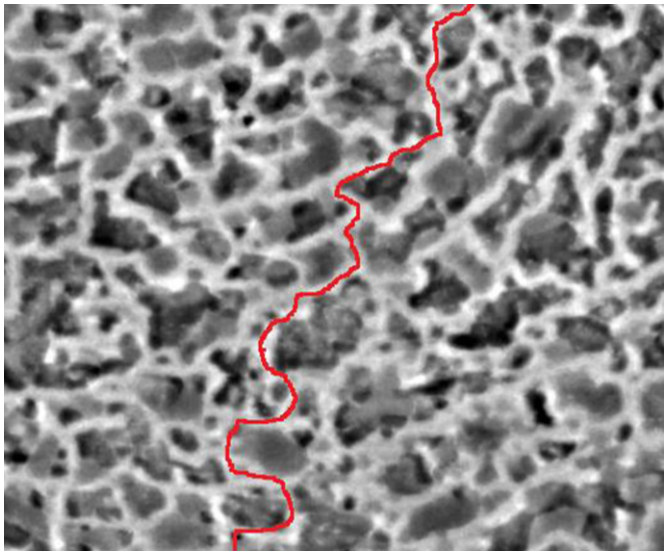

Fig. 10. Schematic of phase-separated Si–Sn nanostructure that presents a torturous path for microcrack propagation.

at different potentials, as shown in the voltage profile (Fig. 5) and d*Q*/d*V* plot (Fig. 8). During discharge (lithiation, voltage curves not shown), the lithium first inserts into the Sn matrix at a higher potential, and then inserts into the nanosized amorphous Si particles. The rapid diffusion of lithium into Sn (characterized by a diffusion coefficient on the order of 10^{-5}–10^{-6} m^2 s^{-1} compared with a value of 10^{-13}–10^{-14} m^2 s^{-1} for a Si host) gives rise to a fast and uniform distribution of Li within the Sn network. This effect helps to reduce the concentration gradient through the film, and, thus, reduces diffusion-induced stress.

The insight gained from the cycling stability of phase-separated nanostructured Si–Sn thin film electrode will assist in designing micron-sized Si–Sn secondary particles suitable for negative electrode materials. These primary particles will have phase separated, nanosegregated Si and Sn. The micron-sized secondary particles would have less surface area, which may reduce the first cycle capacity loss that would occur when only nanosized particles would be used, although power density might be somewhat sacrificed. Nevertheless the high specific capacity from the Si–Sn electrode has the potential to enable high energy batteries suitable for extended range electric vehicles.

5. Summary

In this study, we report a unique nanostructure that was produced by phase separating Si and Sn in a thin film. For an optimum Si/Sn ratio [$Si_{54}Sn_{46}$], where amorphous Si nanoparticles were embedded in the Sn matrix, the electrode showed excellent cycling stability and a specific capacity of 1400 mAh g^{-1}; this behavior is desirable for improving the cell capacity based on current negative electrode and positive electrode materials. The nanostructure also has the potential to mitigate mechanical degradation effects by preventing the generation and propagation of microcracks within the electrodes during lithiation.

Acknowledgement

The authors would like to thank Mr. Curtis Wong of GM R&D for SEM characterization.

References

[1] U. Kasavajjula, C. Wang, A.J. Appleby, J. Power Sources 163 (2007) 1003.
[2] A.S. Arico, P. Bruce, B. Scrosati, J.M. Tarascon, W. Schalkwijk, Nat. Mater. 4 (2005) 366.
[3] N. Dimov, in: M. Yoshio, R.J. Brodd, A. Kozawa (Eds.), Lithium-ion Battery: Science and Technology, Springer, 2009.
[4] L.Y. Beaulieu, K.W. Eberman, R.L. Turner, L.J. Krause, J.R. Dahn, Electrochem. Solid-State Lett. 4 (2001) A137.
[5] D. Larcher, S. Beattie, M. Morcrette, K. Edstrom, J.C. Jumas, J.M. Tarascon, J. Mater. Chem. 17 (2007) 3759.
[6] D. Aurbach, J. Power Sources 89 (2000) 206.
[7] C.C. Nguyen, S.-W. Song, Electrochim. Acta 55 (2010) 3026.
[8] J. Graetz, C.C. Ahn, R. Yazami, B. Fultz, Electrochem. Solid-State Lett. 6 (2003) A194.
[9] L.Y. Beaulieu, K.C. Hewitt, R.L. Turner, A. Bonakdarpour, A.A. Abdo, L. Chritensen, K.W. Eberman, L.J. Krause, J.R. Dahn, J. Electrochem. Soc. 150 (2003) A149.
[10] J.R. Dahn, R.E. Mar, M.D. Fleischauer, M.N. Obrovac, J. Electrochem. Soc. 153 (2006) A1211.
[11] C.E. Krill, R. Birringer, Philos. Mag. A 77 (1998) 621.
[12] Y. Idota, T. Kubota, A. Matsufuji, Y. Maekawa, T. Miyasaka, Science 276 (1997) 1395.
[13] I.A. Courtney, J.S. Tse, O. Mao, J. Hafner, J.R. Dahn, Phys. Rev. B 58 (1998) 15583.
[14] M. Winter, J.O. Besenhard, Electrochim. Acta 45 (1999) 31.
[15] L.Y. Beaulieu, T.D. Hatchard, A. Bonakdarpour, M.D. Fleischauer, J.R. Dahn, J. Electrochem. Soc. 150 (2003) A1457.
[16] X. Xiao, P. Liu, M.W. Verbrugge, H. Haftbaradaran, H. Gao, J. Power Sources 196 (2011) 1409.
[17] S. Chao, Y. Yen, Y. Song, Y. Chen, H. Wu, N. Wu, Electrochem. Commun. 12 (2010) 234.
[18] H. Haftbaradaran, J. Song, W.A. Curtin, H. Gao, J. Power Sources 196 (2011) 361.
[19] Y.T. Cheng, M.W. Verbrugge, J. Electrochem. Soc. 157 (2010) A508.
[20] M.W. Verbrugge, Y.T. Cheng, J. Electrochem. Soc. 156 (2009) A927.